

# LIGHT BENDING SCENARIO FOR ACCRETING BLACK HOLES IN X-RAY POLARIMETRY

M. DOVČIAK<sup>1,5</sup>, F. MULIERI<sup>2</sup>, R. W. GOOSMANN<sup>3</sup>, V. KARAS<sup>1</sup>, AND G. MATT<sup>4</sup>

*Draft version January 12, 2013*

## ABSTRACT

We discuss a model of an X-ray illuminating source above an accretion disk of a rotating black hole. Within the so called lamp-post scheme we compute the expected (observed) polarization properties of the radiation reaching an observer. We explore the dependencies on model parameters, employing Monte Carlo radiation transfer computations of the X-ray reflection on the accretion disk and taking general relativity effects into account. In particular, we discuss the role of the black hole spin, of the observer viewing angle, and of the primary X-ray source distance from the black hole. We give several examples of the resulting polarization degree for two types of exemplary objects – active galactic nuclei and Galactic black holes. In order to assess potential observability of the polarization features, we assume the sensitivity of the proposed New Hard X-ray Mission (NHXM).

We examine the energy range from several keV to  $\sim 50$  keV, so the iron-line complex and the Compton hump are included in our model spectra. We find the resultant polarization degree to increase at the higher end of the studied energy band, i.e. at  $\gtrsim 20$  keV. Thus, the best results for polarimetry of reflection spectra should be achieved at the Compton hump energy region. We also obtain higher polarization degree for large spin values of the black hole, small heights of the primary source, and low inclination angles of the observer.

*Subject headings:* polarization — relativistic processes — X-rays: galaxies — X-rays: binaries

## 1. INTRODUCTION

In active galactic nuclei (AGN) and Galactic black holes (GBH), X-rays are produced near the black hole horizon (Frank et al. 2002). The spectrum of these objects typically consists of several constituents, namely, a multi-color thermal component arising from an optically thick accretion disk and a power-law component, thought to originate in an optically thin medium, a.k.a. a ‘corona’ (e.g., Blandford et al. 1990; Krolik 1999). A plausible scheme suggests that the latter component is produced in a hot Comptonizing layer above the disk. Various spectral features originate by the mutual interaction of the accretion disk medium and the corona. In particular, very prominent are the reflection features of iron, which occur in the 6–7 keV range in the local frame of the emitting material (Remillard & McClintock 2006; Fabian 2008).

The mutual proportions among these components in a particular object depend on the physical (spectral) state of the system, as well as the intervening medium along the line of sight. These proportions are also influenced by strong gravity near the black hole, where light bending effects and energy shifts can play a significant role. Disentangling the observed spectrum into its individual components is not a straightforward task, as it poses a degenerate problem and does not generally allow us to constrain all parameters. Nevertheless, accurate determination of the spectral components is an essen-

tial step in measuring the black hole spin, which is one of the most important challenges in the present-day astrophysics of accreting black holes (Fabian et al. 2004). It has been proposed that X-ray polarimetry could provide additional constraints on the accretion disk models, limit the range of acceptable parameter values, and help us reducing the ambiguities that cannot be resolved by spectroscopy alone (Dovčiak et al. 2008; Li et al. 2009; Schnittman & Krolik 2009).

In the inner regions of black hole accretion disks, emerging photons are strongly influenced by strong gravity (Kato et al. 1998). The framework of General Relativity (GR) is needed to properly determine the resulting spectrum (Fabian et al. 2000; Karas 2006; Matt 2006; Miller 2007). Relativistic effects include the energy shifts, both due to special relativity (Doppler effect) and GR (gravitational redshift), as well as the light bending aberration effects that are particularly prominent near the photon orbit:  $r_{\text{ph}} = 3 GM/c^2 = 4.43 M/M_{\odot}$  km for a non-rotating black hole (the radius of  $r_{\text{ph}}$  decreases with the black hole spin increasing). The relevance of GR effects is even more pertinent for the calculations of the observed polarimetric quantities (Connors & Stark 1977; Connors et al. 1980; Laor et al. 1990; Matt 1993; Agol & Krolik 2000; Dovčiak et al. 2004b, 2008; Li et al. 2009; Schnittman & Krolik 2009, 2010). This is mainly due to sensitivity of the polarimetry parameters to the geometrical arrangement of the source.

In Dovčiak et al. (2004b), we studied the GR effects on the polarization properties of the radiation reflected by an accretion disk near a rotating (Kerr) black hole. We considered illumination of the disk surface by a hot corona. The corona acts, via the inverse Compton effect, on thermal disk photons and it produces as an outcome the above-mentioned power-law component.

In this context, a special scheme has been dubbed the

<sup>1</sup> Astronomical Institute, Academy of Sciences, Boční II, CZ-14131 Prague, Czech Republic

<sup>2</sup> Istituto di Astrofisica Spaziale e Fisica Cosmica, Via del Fosso del Cavaliere 100, I-00133 Rome, Italy

<sup>3</sup> Observatoire Astronomique de Strasbourg, 11 rue de l’Université, F-67000 Strasbourg, France

<sup>4</sup> Dipartimento di Fisica, Università degli Studi “Roma Tre”, Via della Vasca Navale 84, I-00146 Rome, Italy

<sup>5</sup> dovciak@astro.cas.cz

‘lamp-post model’ (Matt et al. 1991; Martocchia & Matt 1996; Henri & Petrucci 1997; Martocchia et al. 2000; Miniutti & Fabian 2004; Dovčiak et al. 2004b). According to this model, the illumination is caused by a point-like source located on the rotation axis of the black hole, which is also the accretion disk axis. This kind of a source can be identified, e.g., with the base of a jet, although the exact interpretation of the ‘lamp’ does not need to be specified at this stage of the phenomenological scenario. Generalizations of the lamp-post model to the case of extended sources, off-axis illumination, and non-planar disks have been also investigated (Dabrowski & Lasenby 2001; Niedźwiecki & Życki 2008). Different, but also highly relevant and interesting geometry of an extended corona has been recently studied by Schnittman & Krolik (2010), taking into account relativistic effects and even the self-irradiation of an accretion disk by its own returning radiation.

The motivation for the present paper arises from the advent of X-ray polarimetry in the field of AGN and GBH (Bellazzini et al. 2006; Bellazzini & Spandre 2010). The paper revisits the light bending scenario of accreting black holes and it improves the calculations of the flux and polarization of the reflected disk emission, with the emphasis on the observability of GR effects and the possibility to constrain the model parameters with future X-ray polarimeters on-board satellites, such as the currently proposed New Hard X-ray imaging and polarimetric Mission (NHXM) (Tagliaferri et al. 2010a,b), or the confirmed Gravity and Extreme Magnetism SMEX (GEMS) mission (Swank et al. 2010).

The paper is organized as follows. In section 2 we briefly introduce the lamp-post scheme for black-hole accretion disks. In section 3 we describe the primary component which acts as a source of the X-ray irradiation. Here we also provide the relevant equations and we calculate the illumination of the disk. In section 4 we describe details of the radiation transfer computation that we apply in order to derive the reflection component. These considerations are then employed in section 5, where we discuss a consistent procedure connecting the primary source position on the rotation axis near the horizon with the signal observed at arbitrary direction far from the black hole. Results for the predicted polarization properties are then described in section 6, taking into account the continuum together with the iron line features. Finally, in section 7 we describe the observational prospects with the currently planned X-ray polarimetric missions. We demonstrate the observability of GR polarimetric features by modeling the expected data from two proto-typical sources and assuming the sensitivity of the NHXM polarimeter as an example. Section 8 summarizes the main results and concludes the paper.

## 2. THE LAMP-POST MODEL FOR BLACK-HOLE ACCRETION DISKS

The lamp-post model was originally proposed by Matt et al. (1991) and Petrucci & Henri (1997) with the aim to provide a simple common scheme for the origin of the X-ray power-law continuum and the relativistic spectral features seen in accreting black hole sources. A natural motivation for this scenario arises from the presumed co-existence of gaseous medium in different states in the inner regions of the accretion disks, and hence

the action of different radiation processes that shape the resulting spectra. This relates, in particular, to the spectrum expected from a geometrically thin, optically thick accretion disk, surrounded by a hot, diluted corona, possibly with an outgoing jet in some objects.

The light-bending scenario was applied by Miniutti & Fabian (2004) to explain the time behavior of the primary and the reprocessed emission of the proto-typical Seyfert 1 galaxy, MCG-6-30-15, where the spectral features from the reprocessing vary less than the primary X-ray continuum. These authors notice that, if the source of primary illumination is located very close to the black hole, the observed spectral properties may result as consequence of rearrangements of the geometrical proportions of the object. This can be interpreted in terms of a point-like source, representing, for example, shocks in the base of a jet, or the location where intense flares arise via magnetic reconnection processes. Rossi et al. (2005) showed, using RXTE data for the X-ray transient XTE J1650-500, that the light bending scheme may well apply also to Galactic black hole systems.

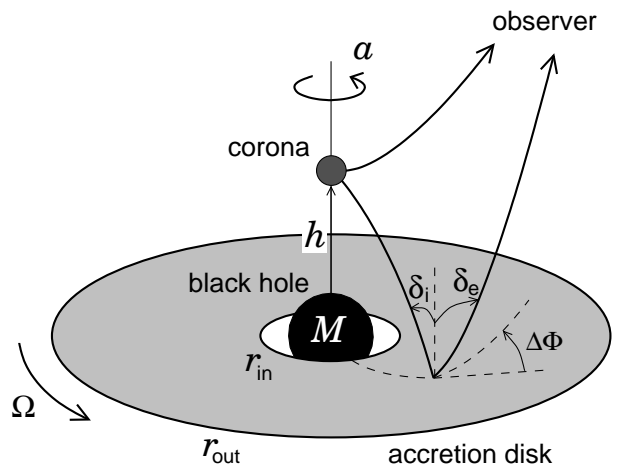


**Figure 1.** Scheme of the model. An elevated primary source situated on the axis of the black hole at height  $h$  illuminates the corotating accretion disk. The observer at infinity receives both the unpolarized power-law radiation from the lamp-post as well as the polarized reflected light from the disk. The incident angle,  $\delta_i$ , between the incoming light ray and the disk normal, the emission angle,  $\delta_e$ , between the outgoing light ray and the disk normal, and the relative azimuthal angle,  $\Delta\phi$ , between the incident and emitted light rays define the scattering geometry in the local frame co-moving with the accretion disk. The normal to the disk and incident and emitted light rays projected onto the disk surface are depicted by the dashed lines.

According to the original, most simple version of this model, the primary ‘lamp’ moves along the black hole axis, typically at heights of only  $\sim 10$ – $20$  gravitational radii above the disk plane. The directly seen continuum component then changes its flux very prominently, mainly due to the effect of changing the gravitational redshift. On the other hand, the reprocessing spectral features are less variable, therefore reproducing the observed pattern, which otherwise is difficult to apprehend. This scheme is attractive because it allows us to connect the black hole parameters to the observed spectral variations, and so it has been pursued in a number of papers.

The above-mentioned interpretation, however, imposes the right proportions between the source height and the accretion disk size, so that the light-bending effect operates efficiently in the desired way. This may not be generally satisfied, or it may be unlikely to happen in majority of sources. The check can be performed by comparing results of various approaches, such as timing, broad-band spectra, and polarimetry. Recently, the rms variability of MCG-6-30-15 was investigated by Niedźwiecki & Miyakawa (2010) and the Suzaku broad-band spectra were discussed by Życki et al. (2010). These authors indeed find various complications that appear when the simple lamp-post scenario is applied to complex data.

The basic definition of the model set-up follows Dovčiak et al. (2004b), see Figure 1. A point-like emitting source on the black hole axis is located at the height  $h$ . The primary emission that is assumed to be unpolarized illuminates the accretion disk where it is reprocessed and part of it is emitted towards the observer. In the lamp post scenario the path of the light that travels from the lamp-post through some point in the disk up to the observer is set for each position on the disk unambiguously, thus defining the scattering geometry at every point in the disk plane, see Figure 1. In this paper we consider only direct photons, i.e., we assume optically thick disk and we neglect the photons that might bend near the photon orbit in such a way that they would circle around the black hole and only then either reach the observer or strike the surface of the disk.

We introduce a number of improvements in addition to our previous polarization computations (Dovčiak et al. 2004b):

- The reflection emission is computed with a more sophisticated multi-scattering Monte Carlo code for the radiation transfer in the accretion disk. As a result of this modeling,
  - the azimuthal dependence of the emission is taken into account (i.e., the reflection dependence on the azimuthal directions between incident and emitted light rays);
  - the reflection is computed also for higher energies (up to 100 keV locally measured energy) and the resulting Compton hump is included in these new computations.
- We have further refined the computation of light geodesics from the axis to the disk plane, and further to the observer, so additional improvements as opposed to our previous results were achieved, especially
  - self-consistent computations for different spin values ( $a = 0.9987$  in our previous work);
  - an extended range of possible heights of the primary source on the axis (we are able to trace the dependence on the height more precisely);
  - geodesics from the axis to the observer are treated in a proper way, i.e., the lensing effect is included (however, we find that the previous

approximation was already very good and this point does not lead to much different results).

- We also include a contribution to the total signal from unpolarized fluorescent  $K\alpha$  and  $K\beta$  lines.

We calculated the flux and polarization of the reprocessed emission, as well as the flux of the direct emission, in four energy bands (2–6 keV, 6–10 keV, 10–20 keV, 20–50 keV) for three different inclination angles (30, 60, and 80 degrees, respectively), and for various values of the height  $h$ . Two different values of the angular momentum of the black hole have been explored: a static,  $a=0$ , and an extremely rotating black hole,  $a=1$ , where, as customary,  $a$  indicates the angular momentum per unit mass in units of the gravitational radius. We use these units for the remainder of this paper. The accretion disk in our computations extends from the marginally stable orbit ( $r_{\text{in}} = r_{\text{ms}}$ ) up to the radius  $r_{\text{out}} = 1000 GM/c^2$ .

### 3. PRIMARY SOURCE, OBSERVED PRIMARY RADIATION, AND ILLUMINATION OF ACCRETION DISK

We assume the primary source of unpolarized radiation to be a point-like patch of the corona located at height  $h < 100$  above the black hole (measured from the center). It radiates isotropically with the specific intensity being the usual power-law dependence on the energy,  $I_{\text{lamp}}(E) = N_{\text{lamp}} E^{-\alpha}$ . In our computations we use the value of the power-law index  $\alpha = 1$  and the normalization factor  $N_{\text{lamp}}$  to be unity in the local static frame.

The primary emission received by the observer gets diluted by the relativistic effects that act on photons on their path, mainly near the central compact body. The observed intensity,  $I_{\text{prim}}(E) \equiv dE/(dt d\Omega d\nu)$ , will be again a power-law in the observed energy

$$I_{\text{prim}}(E) = N_{\text{prim}} E^{-\alpha}, \quad (1)$$

where

$$N_{\text{prim}} = g_{\text{prim}}^{\alpha+1} \frac{d\Omega_{\text{lamp}}}{d\Omega_o} = \left(1 - \frac{2h}{h^2 + a^2}\right)^{\frac{\alpha+1}{2}} \frac{\sin \theta_{\text{lamp}}}{\sin \theta_o} \frac{d\theta_{\text{lamp}}}{d\theta_o}, \quad (2)$$

with  $\theta_{\text{lamp}}$  and  $\theta_o$  being the local emission angle and the inclination angle of the observer, respectively, both measured with respect to the system axis. We denoted the energy shift (from  $E_{\text{lamp}}$  to  $E_{\text{prim}}$ ) of the primary photons detected by the observer by  $g_{\text{prim}} = E_{\text{prim}}/E_{\text{lamp}} = 1/U_{\text{lamp}}^t(h, a) = -g_{tt}^{1/2}(h, a)$ . Here,  $U_{\text{lamp}}^\mu$  is the four-velocity of the motionless lamp-post and  $g_{\mu\nu}$  is the space-time metric. In Figure 2 we show the dependence of the factor  $N_{\text{prim}}$  and intensity  $I_{\text{prim}}$  integrated in several energy bands on the height of the lamp-post for Schwarzschild and extreme Kerr black holes. One can see that the relativistic effects for direct radiation become small for heights  $h \gtrsim 100$  and the difference between extremely rotating and non-rotating black holes are well visible only for heights  $h \lesssim 6$ .

Due to the lamp-post geometry and relativistic effects, the primary source illuminates the accretion disk unevenly. The reflected flux from the disk is proportional to the incident flux on the disk. The incident flux is also the

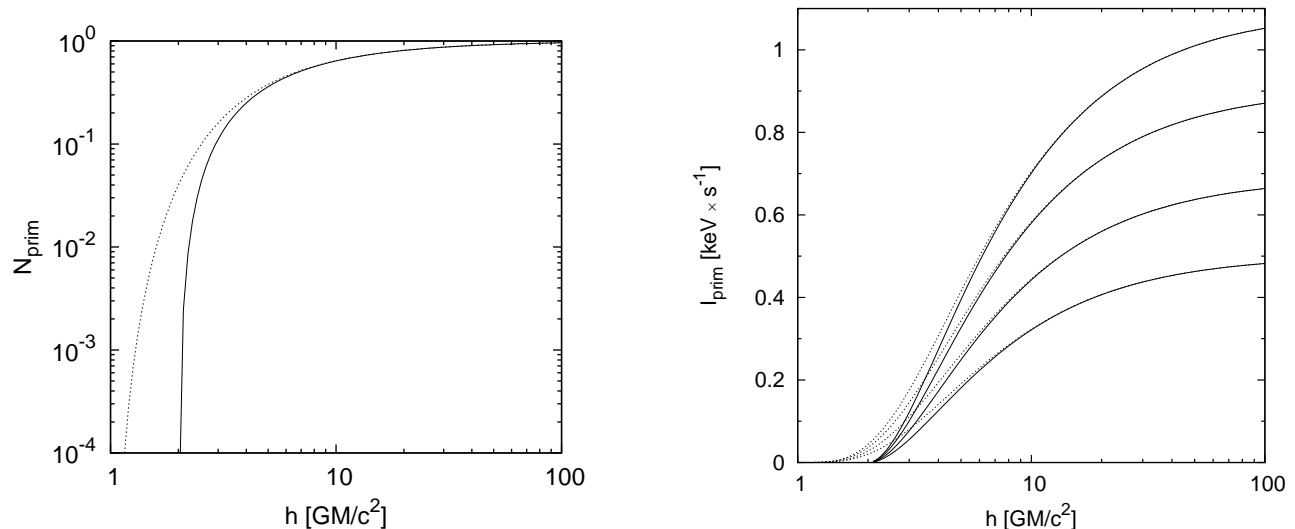


**Figure 2.** Primary emission. *Left:* The emission received by the observer from the primary source is diminished by the factor  $N_{\text{prim}}$  because of the strong gravity of the central black hole. The dependence on the height of the illuminating corona,  $h$ , is shown, if the intensity of the primary power-law emission is  $E^{-1}$ . This factor is almost independent on the inclination of the observer (the curves for inclinations  $1^\circ$  and  $85^\circ$  would be separated by less than the width of the shown curves). *Right:* The primary component of the intensity far from the source (at radial infinity), integrated in the energy ranges 2–6, 6–10, 10–20, and 20–50 keV (curves with higher to lower normalization). The dependence on the height of the primary source is shown with the solid curves for the non-rotating Schwarzschild black hole ( $a=0$ ) and with the dotted curves for the maximally rotating Kerr black hole ( $a=1$ ).

power-law with the same index  $\alpha$  and with the following normalization factor (see Dovčiak et al. 2004b)<sup>6</sup>

$$N_{\text{inc}} = \frac{g_{\text{inc}}^\alpha}{U_{\text{lamp}}^t} \frac{d\Omega_{\text{lamp}}}{dS} = \left( \frac{r^2 + ar^{1/2}}{r\sqrt{r^2 - 3r + 2ar^{1/2}}} \right)^\alpha \left( 1 - \frac{2h}{h^2 + a^2} \right)^{\frac{\alpha+1}{2}} \times \frac{\sin \theta_{\text{lamp}}}{r} \frac{d\theta_{\text{lamp}}}{dr}. \quad (3)$$

Here, the energy shift  $g_{\text{inc}}$  (from  $E_{\text{lamp}}$  to  $E_{\text{inc}}$ ) of the primary photons incident on the accretion disk (measured in local frames) is  $g_{\text{inc}} = E_{\text{inc}}/E_{\text{lamp}} = U_{\text{disk}}^t/U_{\text{lamp}}^t$  with  $U_{\text{disk}}^t$  being the Keplerian four-velocity of the disk. The radial distance  $r$  is the Boyer-Lindquist radial coordinate (we use it here because eventually we integrate in Boyer-Lindquist coordinates on the disk and not in the local frame of the disk). We show the ratio of the incident radiation to that received by the observer directly from the lamp-post in Figure 3.

Compared to the Newtonian case (see the dashed plot in the same figure) this ratio is in both relativistic cases for spinning and non-spinning black holes much larger in the inner accretion disk. The difference between the relativistic and non-relativistic cases increases with the decreasing height of the primary source of radiation. However, we must recall that the incident radiation shown in the figures will still, after it is reprocessed by the disk, undergo some changes on its way from the disk to the observer caused by the relativistic effects. The emission from the vicinity of the black hole horizon will eventually be diminished by the redshift. As a result, for the low

lamp-post heights, the difference between the relativistic and Newtonian ratio of the received direct emission to the received reflected radiation will not be so large.

#### 4. REFLECTED EMISSION

In the equatorial plane of the system we assume a neutral cold geometrically thin and optically thick Keplerian accretion disk. Thus, neutral Fe fluorescent  $K\alpha$  and  $K\beta$  lines are present in the local spectra together with the iron edge. Intensity of the reflected radiation in the local frame co-moving with the accretion disk was computed by the Monte Carlo multi-scattering code **NOAR** (Dumont et al. 2000). Spectral features caused by scattering are hence automatically included in the model spectra, namely, the Compton hump is present; it occurs at energies typically  $\simeq 15$ –50 keV (see example spectra in the left panel of Figure 4).

The normalization of the local flux as well as its shape (mainly in the Compton hump region) depend on the local scattering geometry, i.e., the incident and the emission angles, as well as the relative azimuthal angle of the incident and emitted light rays. We stress the dependence on the incident and relative azimuthal angles of the lamp-post set-up. This feature is additional to the pure directionality dependence on the emission angle in the case of an extended corona when the disk is usually assumed to be illuminated isotropically.

The single scattering approximation (Chandrasekhar 1960) is used for the local polarization of the reflected continuum component (for details see Dovčiak et al. 2004b). The line flux and the primary radiation are supposed to be unpolarized. The polarization properties of the reflected radiation depend highly on the scattering geometry, as is illustrated in Figure 4.

The geometry of scattering is determined by the position where reprocessing happens on the disk. In this set-up the incident and emission angles are decided by the

<sup>6</sup> Note, that we use the power-law index  $\alpha$  for the specific intensity, here, whereas in Dovčiak et al. (2004b) power-law index  $\Gamma$  for the photon number density flux was used.

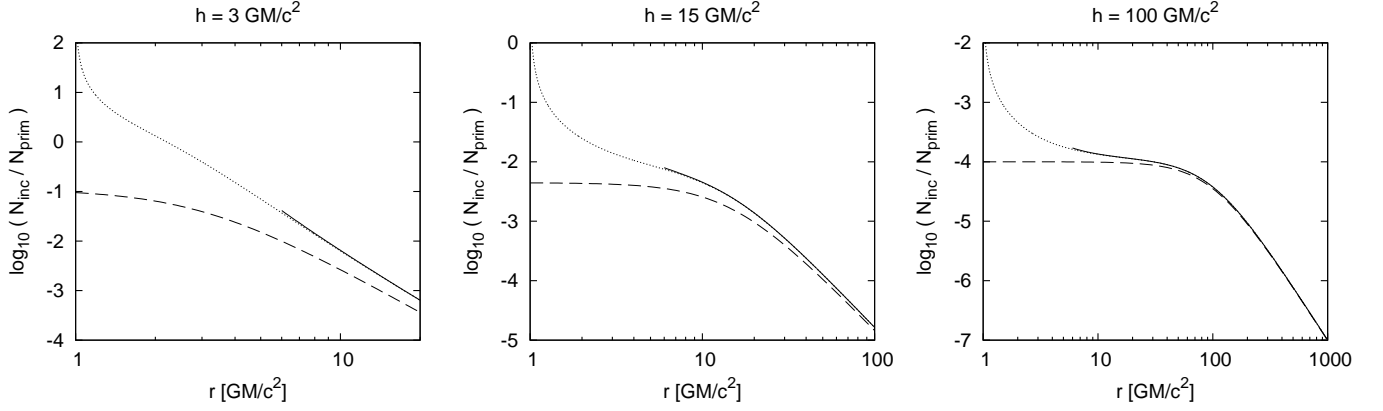


**Figure 3.** Illumination of the disk. The radiation incident on the accretion disk is affected by the relativistic effects. The ratio of the incident radiation to the observed primary emission is shown for three heights of the primary source,  $h = 3, 15$ , and  $100 \text{ GM}/c^2$  (from left to right). The dependence on the radius is shown for the non-rotating Schwarzschild black hole ( $a=0$ ) with the solid curve, for the maximally rotating Kerr black hole ( $a=1$ ) with the dotted curve, and for the Newtonian case with the dashed curve.

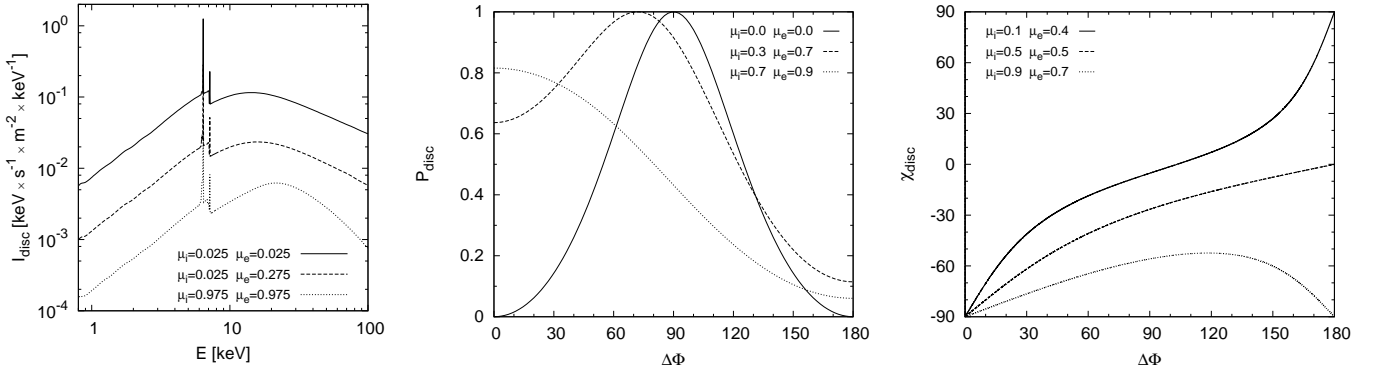


**Figure 4.** Reprocessed radiation. The properties of the local reprocessed radiation depend on the position on the disk. This is due to their dependence on the local scattering geometry. *Left:* The local intensity varies by more than one order of magnitude for different values of incident and emission angles. The shape of the Compton hump changes as well. Examples of spectra for three different pairs of values of the incident and emission cosines,  $\mu_i$  and  $\mu_e$ , are shown. Here we assumed the relative azimuthal angle between incident and emitted light rays to be small ( $\Delta\Phi = 2.5^\circ$ ). *Middle:* The local polarization degree can have any value between 0 and 1. We show the dependence on the relative azimuthal angle  $\Delta\Phi$  for three pairs of incident and emission cosines. *Right:* The local polarization angle obtains any value between  $-90^\circ$  and  $90^\circ$ . The dependence on the relative azimuthal angle  $\Delta\Phi$  for three pairs of incident and emission cosines is shown. A polarization angle of  $0^\circ$  represents the direction perpendicular to the disk.

incoming and outgoing geodesics. Throughout the disk all three angles,  $\delta_i$ ,  $\delta_e$ , and  $\Delta\phi$  (Figure 1), may attain almost all possible values. Thus also the local polarization degree  $P_{\text{disk}}$  and angle  $\chi_{\text{disk}}$  may achieve the whole range of values, 0 to 1 and  $-90^\circ$  to  $90^\circ$ , respectively, as is illustrated in Figure 4. In our computations, a polarization angle of  $0^\circ$  always represents the direction perpendicular to the disk and it is rotated counter-clockwise for positive values when looking towards the approaching photon.

##### 5. RADIATION FAR FROM SOURCE

To get the resultant polarization far from the source, i.e. at radial infinity, one has to integrate the emission over the disk surface and thus one integrates the local polarization properties. From the previous section it is obvious that the result of such integration is not easily estimated because of the complicated dependence on the local geometry of scattering. Moreover, relativistic effects enhance radiation from some parts of the disk. They also rotate the polarization angle, and thus the overall observed polarization properties will be given by an interplay of the local polarization properties on the

disk and relativistic change acting on photons on their way to the observer.

From our previous studies of polarization of thermal radiation of the accretion disk (see Dovčiak et al. 2008) one expects relativistic depolarization of the local polarization. This depolarization should be larger for a spinning black hole when the inner part of the accretion disk extends closer to the horizon, and thus is larger in size when compared to the Schwarzschild non-rotating case where there is a large central hole in the disk. It is in this inner part where the relativistic rotation of the polarization angle is the most variable. Yet, in the lamp-post geometry we may get different results (i.e. higher polarization for higher spin) when the primary radiation is taken into account as well, as we will see later on.

The overall polarization at infinity is given by the Stokes parameters that have to be integrated over the accretion disk surface,

$$\begin{aligned} I_o &= I_{\text{refl}} + I_{\text{prim}} = \\ &= \int_{\Sigma} dS G (I_{\text{disk}}^{\text{cont}} + I_{\text{disk}}^{\text{line}}) + I_{\text{prim}}, \end{aligned} \quad (4)$$

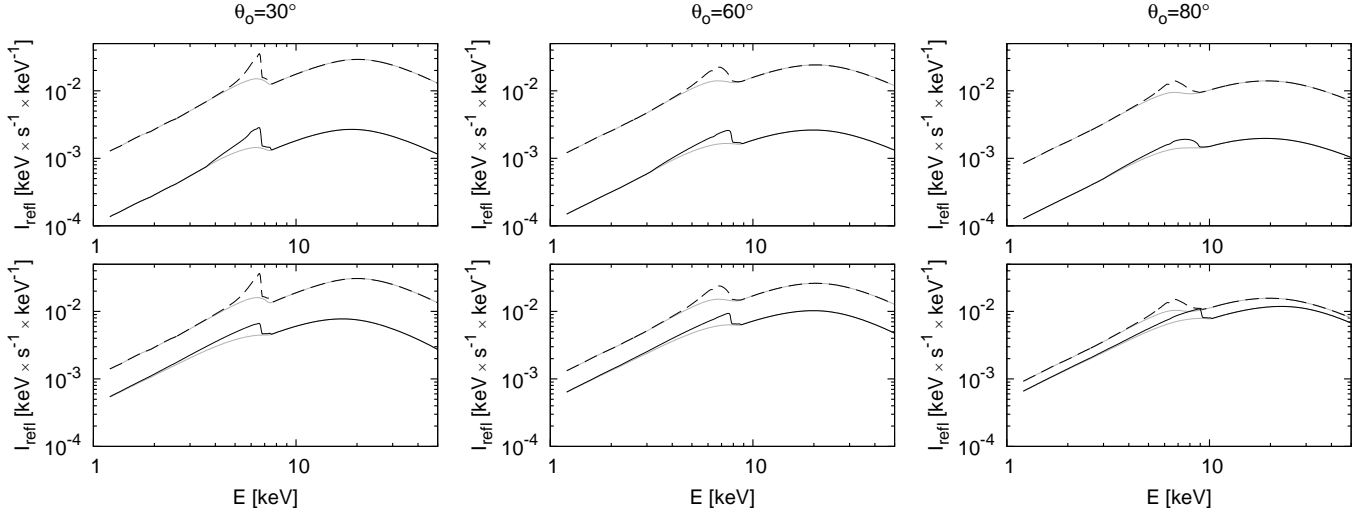


**Figure 5.** Reflected component at infinity. The spectrum of the reflected component as the observer at infinity would measure it for three different inclination angles,  $\theta_o = 30^\circ$ ,  $60^\circ$ , and  $80^\circ$  (from left to right) and two heights of the primary source,  $h = 3 GM/c^2$  (solid) and  $h = 15 GM/c^2$  (dashed). The top panels correspond to the Schwarzschild case ( $a=0$ ), the bottom panels correspond to the extremely rotating Kerr case ( $a=1$ ). The grey lines depict the spectrum when the Fe K $\alpha$  and K $\beta$  lines are omitted.

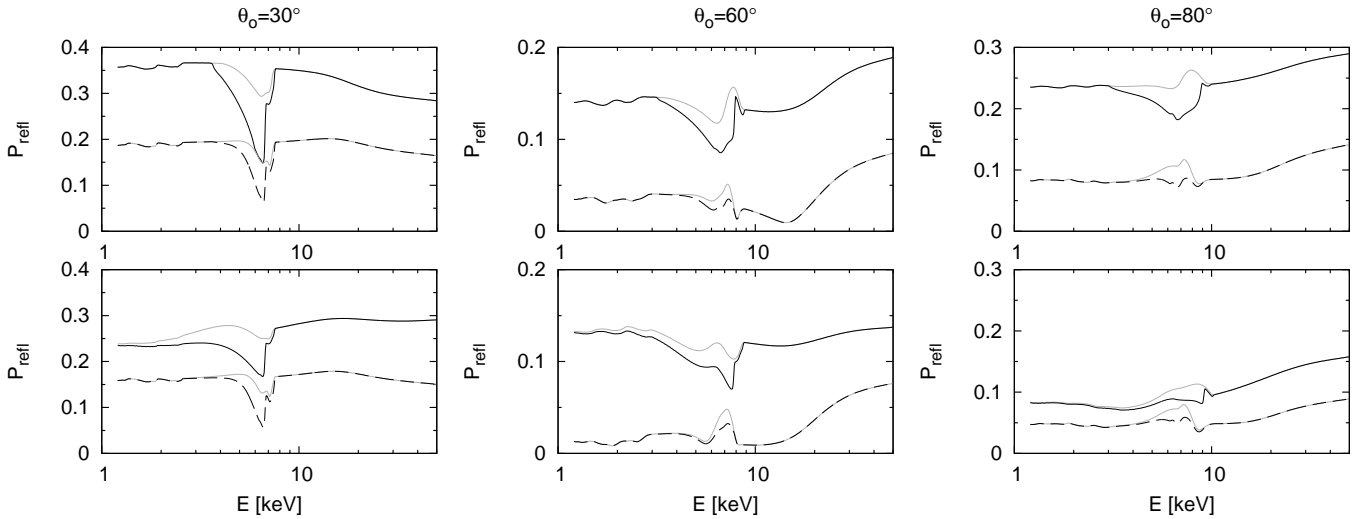


**Figure 6.** Polarization of the reflected component. The polarization of the reflected component as the observer at infinity would measure it for three different inclination angles,  $\theta_o = 30^\circ$ ,  $60^\circ$ , and  $80^\circ$  (from left to right) and two heights of the primary source,  $h = 3 GM/c^2$  (solid) and  $h = 15 GM/c^2$  (dashed). The energy dependence of the polarization degree is shown. The top panels correspond to the Schwarzschild case ( $a=0$ ), the bottom panels correspond to the extremely rotating Kerr case ( $a=1$ ). The grey lines depict the polarization degree if the unpolarized Fe K $\alpha$  and K $\beta$  lines are not considered.

$$Q_o = \int_{\Sigma} dS G P_{\text{disk}} I_{\text{disk}}^{\text{cont}} \cos 2(\chi_{\text{disk}} + \psi), \quad (5)$$

$$U_o = \int_{\Sigma} dS G P_{\text{disk}} I_{\text{disk}}^{\text{cont}} \sin 2(\chi_{\text{disk}} + \psi). \quad (6)$$

Here, the relativistic effects are expressed in terms of the transfer function  $G$  and the relativistic rotation of the polarization angle  $\psi$ . For their definition and behavior see our previous work in Dovčiak (2004); Dovčiak et al. (2004a). We have divided the intensity measured by the observer into the part coming directly from the primary source,  $I_{\text{prim}}$ , and the part reflected by the accretion disk,  $I_{\text{refl}}$ . The latter one can still be divided into the polarized continuum part,  $I_{\text{refl}}^{\text{cont}}$ , and the unpolarized intensity

coming from fluorescent neutral iron lines (K $\alpha$  and K $\beta$ ),  $I_{\text{refl}}^{\text{line}}$ . We denote their counterparts in the local frames in which the radiation is emitted, i.e. before applying relativistic changes, as  $I_{\text{lamp}}$ ,  $I_{\text{disk}}^{\text{cont}}$ , and  $I_{\text{disk}}^{\text{line}}$ , respectively. The observed linear polarization degree  $P_o$  and polarization angle  $\chi_o$  are computed from the Stokes parameters in the usual way, i.e.  $P_o = \sqrt{Q_o^2 + U_o^2}/I_o$  and  $\tan 2\chi_o = U_o/Q_o$ .

## 6. RESULTS

### 6.1. Polarization of the reprocessed radiation and iron line features

First, we will look at the polarization properties of the relativistically broadened iron line. To this purpose we

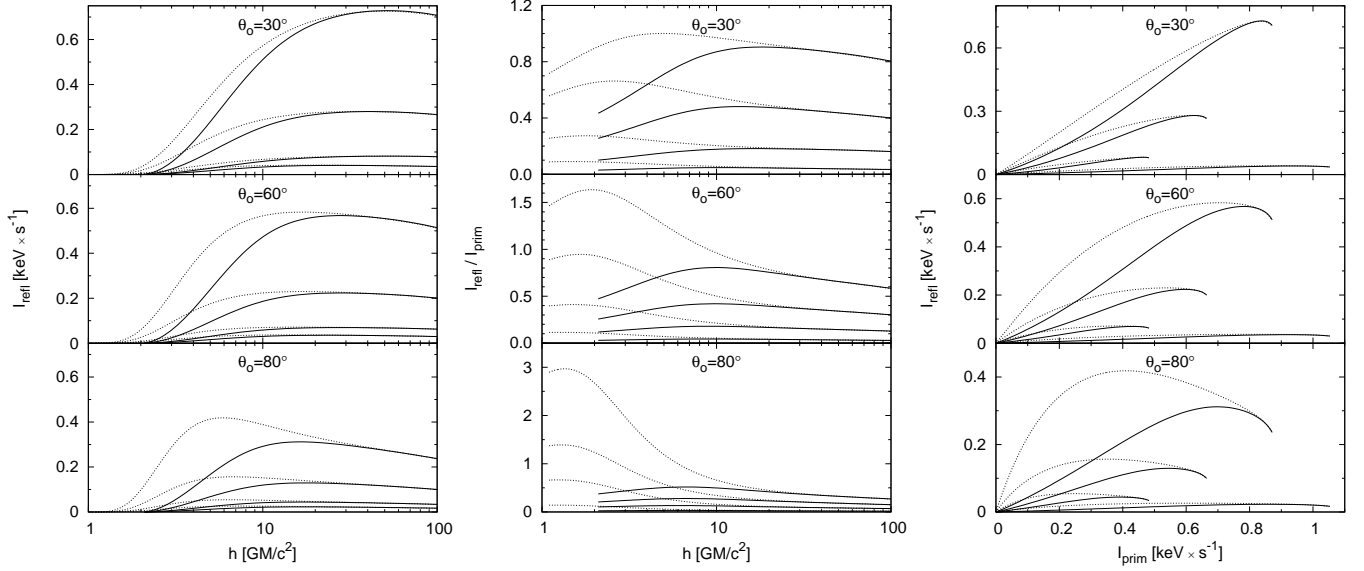


**Figure 7.** Reflected intensity at infinity. *Left:* The reflected component of the intensity at infinity integrated in the energy ranges 2–6, 6–10, 10–20, and 20–50 keV (curves with lower to higher normalization) for three different observer inclinations,  $\theta_o = 30^\circ$ ,  $60^\circ$  and  $80^\circ$  (top to bottom panels). The dependence on the height of the primary source is shown by the solid curve for the non-rotating Schwarzschild black hole ( $a=0$ ) and by the dotted curve for the maximally rotating Kerr black hole ( $a=1$ ). *Middle:* The same as on the left but for the ratio of the reflected to the primary components of the intensity at infinity. *Right:* The same as on the left but for the dependence on the intensity of the primary source as an observer would measure it at infinity. In this graph, the height of the primary source increases with the primary intensity from 0 to  $100 GM/c^2$ .

show only the reflected component of the intensity  $I_{\text{ref}}$  and polarization degree  $P_{\text{ref}}$  (Figures 5 and 6). The value of the polarization angle does neither depend on the primary radiation nor on the intensity of the iron lines, thus we will consider it only in the next section when we will discuss polarization properties with the primary emission taken into account as well.

In Figure 5 one can see typical relativistic reflection spectra with a broad iron line below 10 keV and Compton hump that peaks around 20 keV. Here we show several examples from the lamp-post geometry varying different model parameters – the height of the primary source, the inclination of the observer, and the spin of the black hole. We show also the reflection continuum so that the intensity of the line is emphasized. The line is broader for lower  $h$  of the lamp-post because more photons hit the disk near its inner edge (see Figure 3) where the line is shifted to the lower energy.

Due to the fact that the  $K\alpha$  and  $K\beta$  lines are unpolarized in our model, the polarization degree  $P_{\text{ref}}$  should be reduced at the energies to which the line is shifted. However, in some cases this needs not to be true and there even can be a rise in polarization degree, see the graphs for heights  $h = 15 GM/c^2$  in Kerr case in Figure 6. The reason for this behavior is the presence of the iron edge, where the polarized continuum intensity suddenly drops. As this edge is shifted to different energies there is a change in the contribution of the polarized flux at the energies near it. The overall effect can be either enhancing the polarization or decreasing it (see the grey graphs representing only the continuum emission).

The polarization of the reflected component can be quite high. In our example figures it is the highest at lower energies,  $E \lesssim 4 \text{ keV}$ , for lower heights of the primary source,  $h = 3 GM/c^2$ , low inclination,  $\theta_o = 30^\circ$ ,

and for the Schwarzschild black hole when it is slightly above 35%.

Next we show the reflected emission (Figure 7) as a function of the lamp-post height, for the different energy bands (2–6, 6–10, 10–20, and 20–50 keV), and for the three values of the inclination angle ( $30^\circ$ ,  $60^\circ$ , and  $80^\circ$ ). The reflected radiation first increases with the height, mainly due to the increase of the disk solid angle as seen by the source (i.e. the light-bending effect decreases). Thus for small heights the incident radiation on the disk increases with the height. The decrease at large heights (above  $h \gtrsim 30 GM/c^2$ ) is primarily due to the finite size of the disk in our computations (we used  $r_{\text{out}} = 1000 GM/c^2$ ). However, even if the disk had extended into infinity, there would still have been slight decrease in the reflected intensity with the height, as opposed to the Newtonian case when it should stay constant. This is due to the fact that the reflected radiation from the inner disk is more intense in the relativistic case and as the lamp-post height increases the solid angle of the inner region, where relativity effects are important, decreases.

For very large heights the reflected component approaches the Newtonian case. From Figure 7 (left and middle panels) one can see that the intensity for different spins is almost the same already for heights around  $30 GM/c^2$ , which is also due to the fact that at these heights the innermost accretion disk already makes quite a small contribution to the overall reflected radiation. From the figure it is also apparent that the contribution of the inner disk to the total intensity for the extreme Kerr black hole is the largest for high inclination angles. In Figure 7 we also show the dependence of the ratio of the reflected to the primary intensity on the lamp-post height and reflected versus primary intensity. Note, that

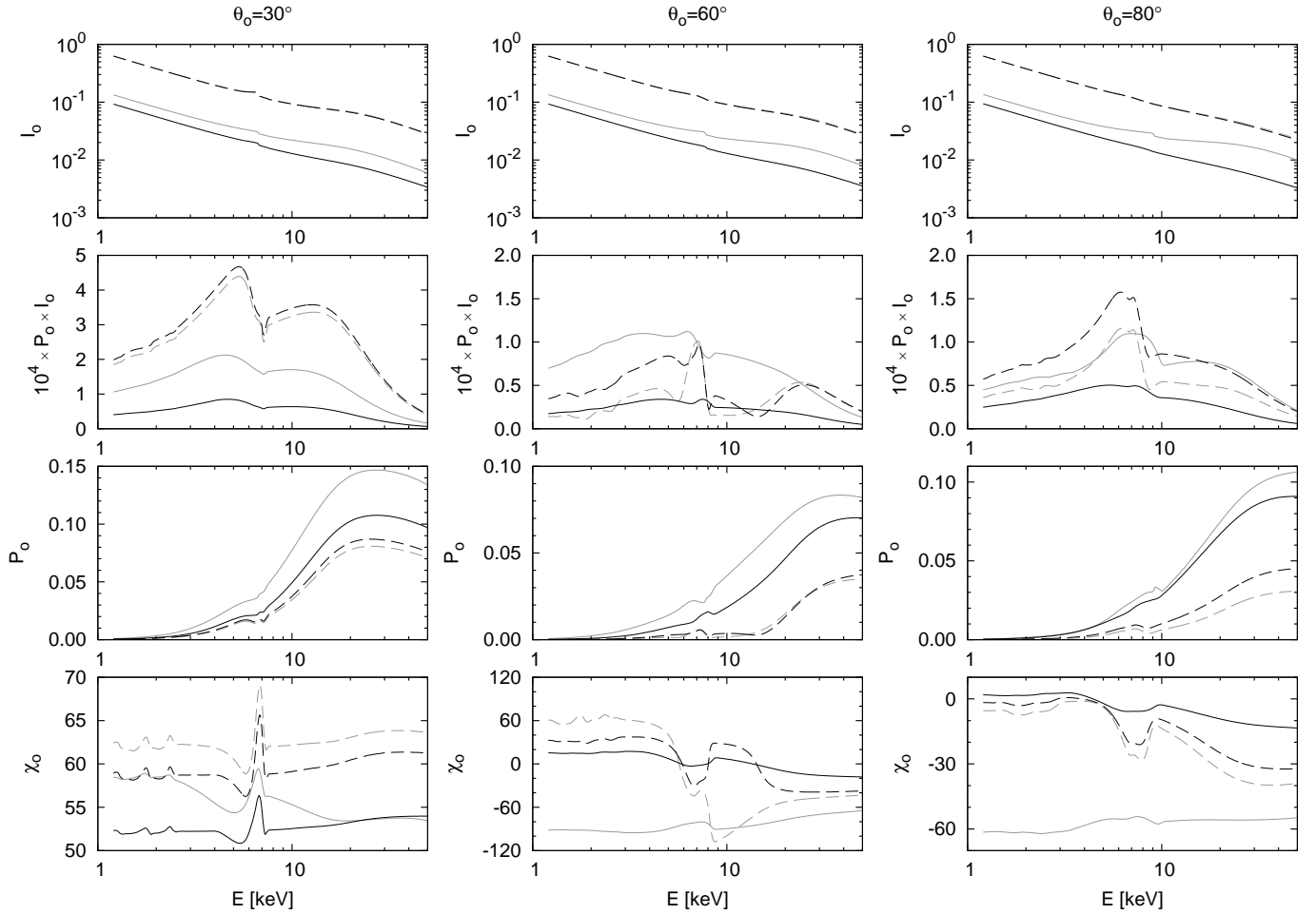


**Figure 8.** Properties of the radiation at infinity. Intensity, polarized intensity, polarization degree, and polarization angle (top to bottom) at infinity for the total radiation, i.e. both primary and reflected components are included. The observer inclination is  $\theta_o = 30^\circ, 60^\circ$ , and  $80^\circ$  (from left to right) and the height of the primary source is  $h = 3 GM/c^2$  (solid) and  $h = 15 GM/c^2$  (dashed). The black graphs correspond to the Schwarzschild case ( $a=0$ ), the grey graphs correspond to the extremely rotating Kerr case ( $a=1$ ).

for low heights the contribution of the reflected component may be even larger than that of the primary one (in higher energy bands). All these effects are qualitatively similar to those described in Miniutti & Fabian (2004), who adopted a somewhat different geometry for the primary source (i.e. a ring centered on the black hole axis).

### 6.2. Overall polarization far from source

If we consider the primary radiation as well, the decrease of the polarization degree in the iron line region is much less visible, because the primary flux at these energies is still large. On the other hand, at high energies, where the contribution from direct radiation is relatively lower and where the Compton scattering increases the contribution of the reflected radiation, the polarization degree increases. We illustrate this behavior in Figure 8 for two values of the lamp-post heights ( $h = 3$  and  $15 GM/c^2$ ). We also show the energy dependence of the polarization angle in the same figure. As previously mentioned for the polarization degree of the reflected component, one can see quite a large effect of the iron edge.

The dependence of the polarization degree and angle at infinity on the lamp-post height, observer inclination, and total intensity at infinity are shown in Figures 9–

12. In all these figures both the reflected and primary emission are considered and the results are computed in several energy bands.

To understand the relativistic results one has to take into account several aspects different from the Newtonian case:

1. *Local polarization.* The emission angle, on which the local polarization properties depend, is not equal to the observer's inclination. Its value depends on the position on the disk from which the photon is emitted. The emission angle is approaching the observer inclination only for large radii. Therefore if the local polarization depended only on the emission angle, it would be the same all over the disk in the Newtonian case whereas it would change considerably in the relativistic case. The local incident angle and relative azimuthal angle between the incident and emitted light rays are different as well.
2. *Transfer function.* The transfer function in the eqs. (4)–(6) acts as a weight that amplifies the emission in some areas on the disk while in other parts it can very efficiently suppress the outcoming ra-



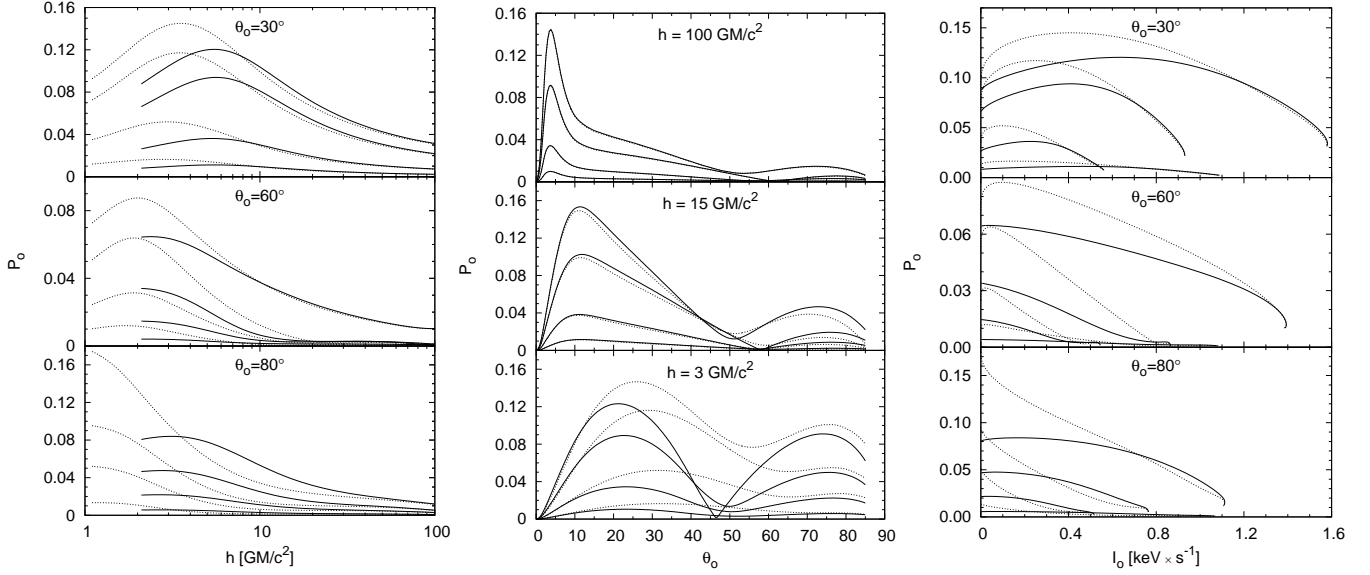


**Figure 9.** Polarization degree at infinity. The values for the energy ranges 2 – 6, 6 – 10, 10 – 20, and 20 – 50 keV (curves with lower to higher normalization) are shown. The solid curves are for the non-rotating Schwarzschild black hole ( $a=0$ ), the dotted curves are for the maximally rotating Kerr black hole ( $a=1$ ). *Left:* The dependence on the height of the primary source for three different observer inclinations,  $\theta_o = 30^\circ$ ,  $60^\circ$ , and  $80^\circ$  (top to bottom panels). *Middle:* The dependence on the observer inclination for three different heights of the primary source,  $h = 100$ ,  $15$ , and  $3 \text{ GM}/c^2$  (top to bottom panels). *Right:* The dependence on the total intensity at infinity for three different observer inclinations,  $\theta_o = 30^\circ$ ,  $60^\circ$ , and  $80^\circ$  (top to bottom panels). In this graph, the height of the primary source increases with the total intensity from 0 to  $100 \text{ GM}/c^2$ .

diation. Due to the relativistic effects this impact is non-axisymmetric. Thus whereas in the Newtonian case the overall polarization angle may be parallel or perpendicular due to the symmetry of the system, this does not apply to the relativistic case where the observed polarization angle may, in principle, attain any value.

3. *Energy dependence.* While in the Newtonian case the energy dependence of the local polarization does not play any important role it is not so in the relativistic case. Due to energy shift of the photons the local intensities in the eqs. (4)–(6) work as weight similarly as the transfer function mentioned above. Thus the features such as the unpolarized iron line, the iron edge and the Compton hump may change the contribution of different parts of the disk to the polarization in a particular energy band, especially if those features are shifted in and out of the energy band of interest.
4. *The dependence of the relativistic rotation of the polarization angle on observer inclination.* To understand this effect one has to realize the role of the critical point, where the photons are emitted perpendicularly to the disk. The existence of this point is due to special relativistic aberration. For small inclinations even very small orbital speed of the matter moving towards the observer is enough to ensure that light rays emitted perpendicularly to the disk reach the observer. For very large inclinations the orbital speed must be much higher. Therefore the critical point is far away from the center for small observer inclinations whereas it moves close towards the center for very high ones. In the latter case the contribution of the general

relativistic aberration and light bending becomes important and as a result the location of the critical point is behind the black hole. For small inclinations the critical point is at the azimuth where the disk is moving towards the observer. For the importance of the special relativistic effects (aberration, Doppler effect and thus special relativistic rotation of the polarization angle) and the general relativistic effects (significant for small radii: light bending, gravitational shift, and general relativistic rotation of polarization angle) see Figure 3 in Dovčiak et al. (2008), Appendix D in Dovčiak (2004), or Figure 1.3 in Dovčiak (2010). One can see there that for radii below the critical radius the relativistic rotation of the polarization angle,  $\psi$ , spans the whole possible range (i.e. from  $-180^\circ$  to  $+180^\circ$ ) whereas above the critical radius the rotation is restricted to some interval that gets quite narrow for large radii.

5. *Spin of the black hole.* The disk around the black hole is supposed to terminate at the marginally stable orbit which means there is a cavity in the disk around the black hole; the lower the black hole spin, the larger the cavity. Because the largest influence of the relativistic effects are visible mainly in close vicinity to the black hole, the relativistic effects are much more pronounced for highly spinning black holes.

As a consequence, different parts of the disk will emit light with different local polarization. The direction of this polarization will be further changed as the photon travels from local frame co-moving with the disk to the stationary observer and this change will be again dependent on the place of the emission. The contribution to

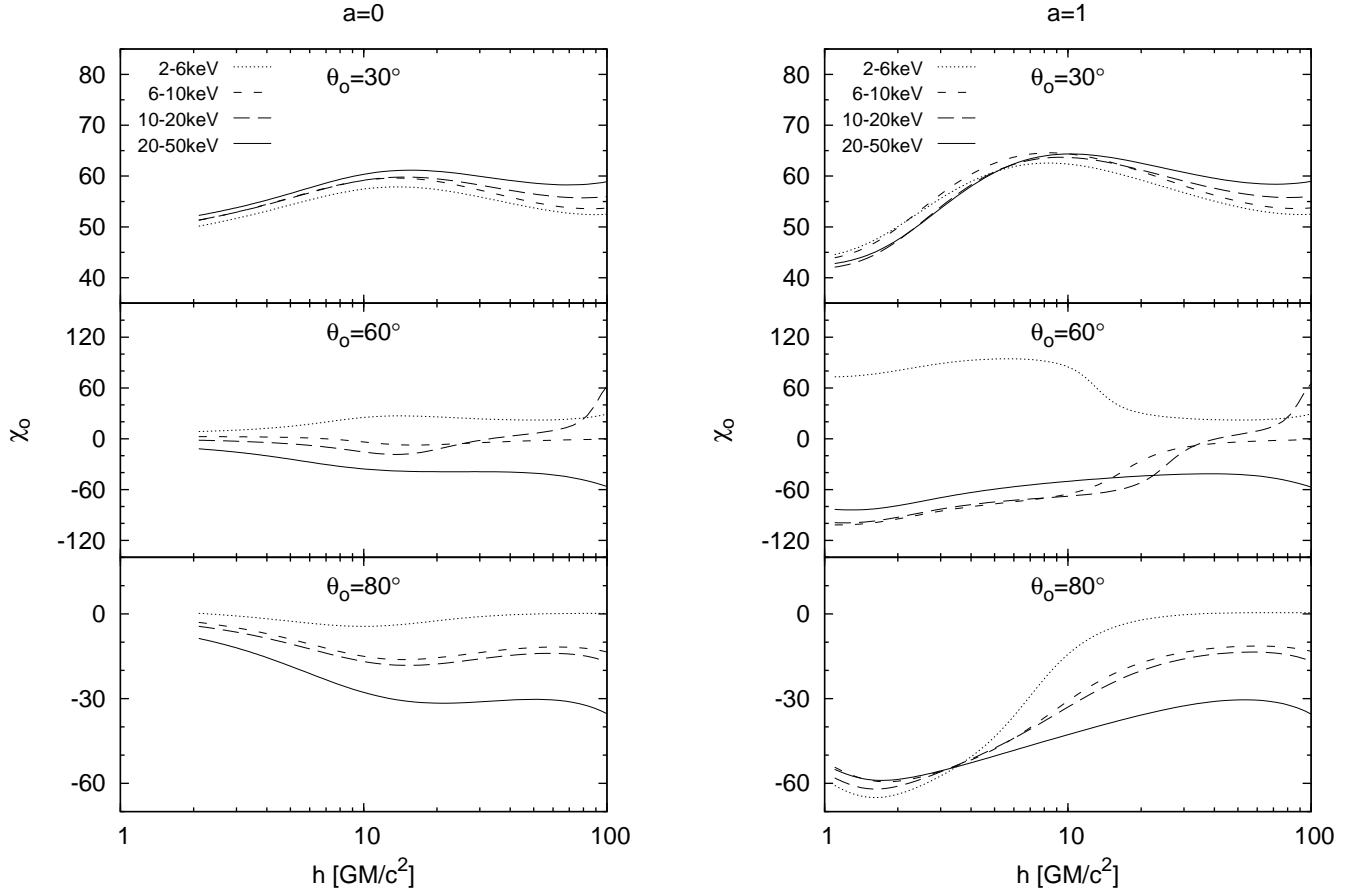


**Figure 10.** Dependence of the polarization angle at infinity on the height of the primary source. A polarization angle of  $0^\circ$  represents the direction perpendicular to the disk. The values for the energy ranges 2–6, 6–10, 10–20, and 20–50 keV for three different observer inclinations,  $\theta_o = 30^\circ$ ,  $60^\circ$ , and  $80^\circ$  (top to bottom panels) are shown. *Left:* The non-rotating Schwarzschild black hole case ( $a=0$ ). *Right:* The maximally rotating Kerr black hole case ( $a=1$ ).

the overall polarization from each part of the disk will be different depending on the weight given by the transfer function and the local intensity (both dependent on the position on the disk). The latter one is proportional to the incident intensity from the primary source thus the height of the lamp determines at which radii the disk shines the most. The incident angle under which photons strike the surface of the disk also depends on the height of the lamp, so the height modifies the local polarization degree and angle as well.

Thus while in the Newtonian case it is quite straightforward to see how the polarization by reflection from the disk behaves it is much more complicated in the relativistic case. Therefore, in the following, we will restrict ourselves to the description of the most interesting results and we will discuss only the main qualitative features.

We begin with a bit surprising and contra-intuitive result — the polarization degree is highest when the radiation from the inner accretion disk has a large contribution to the overall flux. This is opposite to the de-polarization one gets in the inner disk for the Comptonized thermal radiation, (see Dovčiak et al. 2008; Schnittman & Krolik 2009). The cause of the thermal de-polarization is the relativistic rotation of the polarization angle. The local polarization is in this case always either parallel or perpendicular to the disk. In the reflection model the local

polarization angle depends on the local scattering geometry. When integrating the contributions from the disk, the local polarization angle adds up with the relativistic rotation in such a way that the overall polarization is much less de-polarized.

This has two consequences. Firstly, the highest polarization degrees are achieved for low lamp-post heights when the inner region of the disk is more illuminated than its more distant parts. Secondly, the radiation from the extreme Kerr black-hole accretion disk is more polarized than that in the Schwarzschild case where there is a hole in the disk below marginally stable orbit. Note, however, that there are some exceptions to the latter behavior, see the results for some intervals of the lamp-post heights and for the observer inclination  $30^\circ$  and  $80^\circ$ . This can be explained by the fact that the polarization in the Schwarzschild case is determined only by the disk above marginally stable orbit,  $r > r_{\text{ms}} = 6GM/c^2$ , while in the Kerr case the contribution from the disk below and above this radius have different polarizations, effectively reducing the overall polarization.

Note, that in Kerr case the dependence of the polarization degree on the height, Figure 9, roughly follows the dependence of the ratio of the reflected and primary radiation,  $I_{\text{refl}}/I_{\text{prim}}$ , see middle panel in Figure 7. This is not true for the Schwarzschild black hole where for low

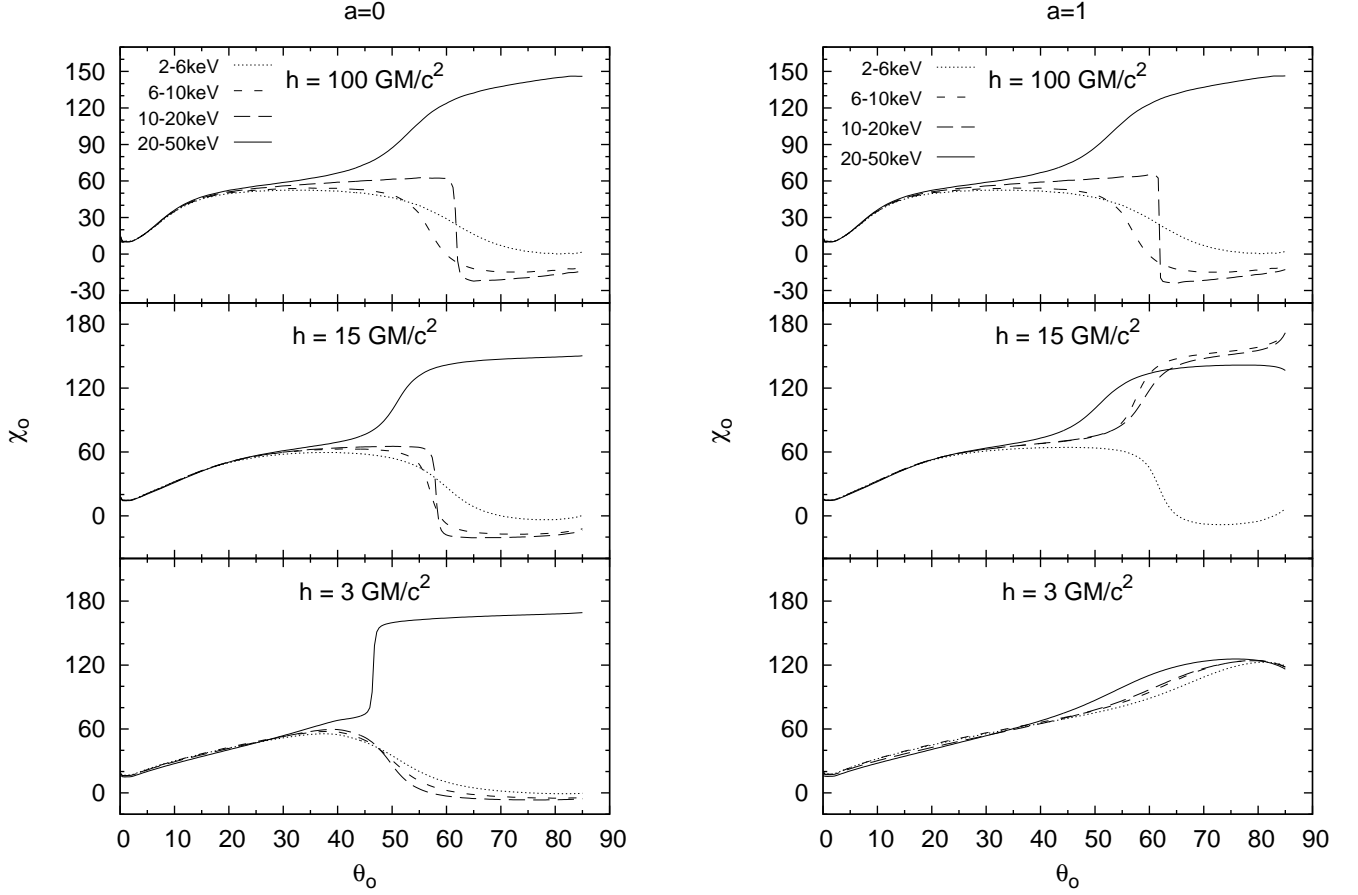


**Figure 11.** Dependence of the polarization angle at infinity on the observer inclination. A polarization angle of  $0^\circ$  represents the direction perpendicular to the disk. The values for the energy ranges 2–6, 6–10, 10–20, and 20–50 keV for three different heights of the primary source,  $h = 100, 15$ , and  $3 \text{ GM}/c^2$  (top to bottom panels) are shown. *Left:* The non-rotating Schwarzschild black hole case ( $a=0$ ). *Right:* The maximally rotating Kerr black hole case ( $a=1$ ).

lamp-post heights the polarization is quite large in spite of the fact that the reflected intensity is much smaller (due to the missing innermost part of the disk). This, again, is just another consequence of the fact that the contribution of the inner disk above the marginally stable orbit to the overall observed polarization is significant.

We should also mention that similarly to the intensity also the polarization degree and angle do not change with the spin for large heights ( $h \gtrsim 30 \text{ GM}/c^2$ ) of the primary source (see left panel in Figure 9 and both panels in Figure 10).

The polarization degree has a maximum for low observer inclinations, e.g. in the highest studied energy band, 20–50 keV, for the lamp-post height  $h = 3 \text{ GM}/c^2$  it peaks in the extreme Kerr case at inclination  $25^\circ$  where it reaches almost 15% polarization (see the middle panel in Figure 9).

The polarization degree for zero inclination angle has to be zero because of the symmetry. As soon as the symmetry is broken by non-zero inclination the total polarization increases, determined by the region below critical radius which for low inclinations is far from the center. As soon as the emission above this radius starts to contribute significantly the overall polarization starts to decrease with the inclination angle (the larger the inclination the lower the critical radius). This turn-around is at

lower inclinations for larger heights because higher lamp-post illuminates better farther radii (i.e. radii above the critical one). There is another turn-around at the inclination when the critical radius moves close to the center. The contribution to the polarization from below and above critical radius cancel each other and the dependence of the polarization degree on the observer inclination reaches its minimum. For even higher inclinations the polarization again increases, it is determined mainly by the emission from far above the critical radius with lower and lower contamination from the regions around and below this radius. For very high inclinations the reflection is small and thus the overall polarization decreases again.

The polarization angle at infinity is quite sensitive to the details described in the points mentioned above and its dependence on height and inclination is rather complex. Note mainly the different behavior in different energy bands (Figures 10–11). While the polarization degree behaves in different energy bands very similarly, just being scaled up with higher energy, the polarization angle dependences may differ substantially. As discussed above for the polarization degree, the polarization angle for low inclinations is also determined mainly by the region below critical radius (top panels in Figure 10) while for high inclinations by the region above this radius (mid-

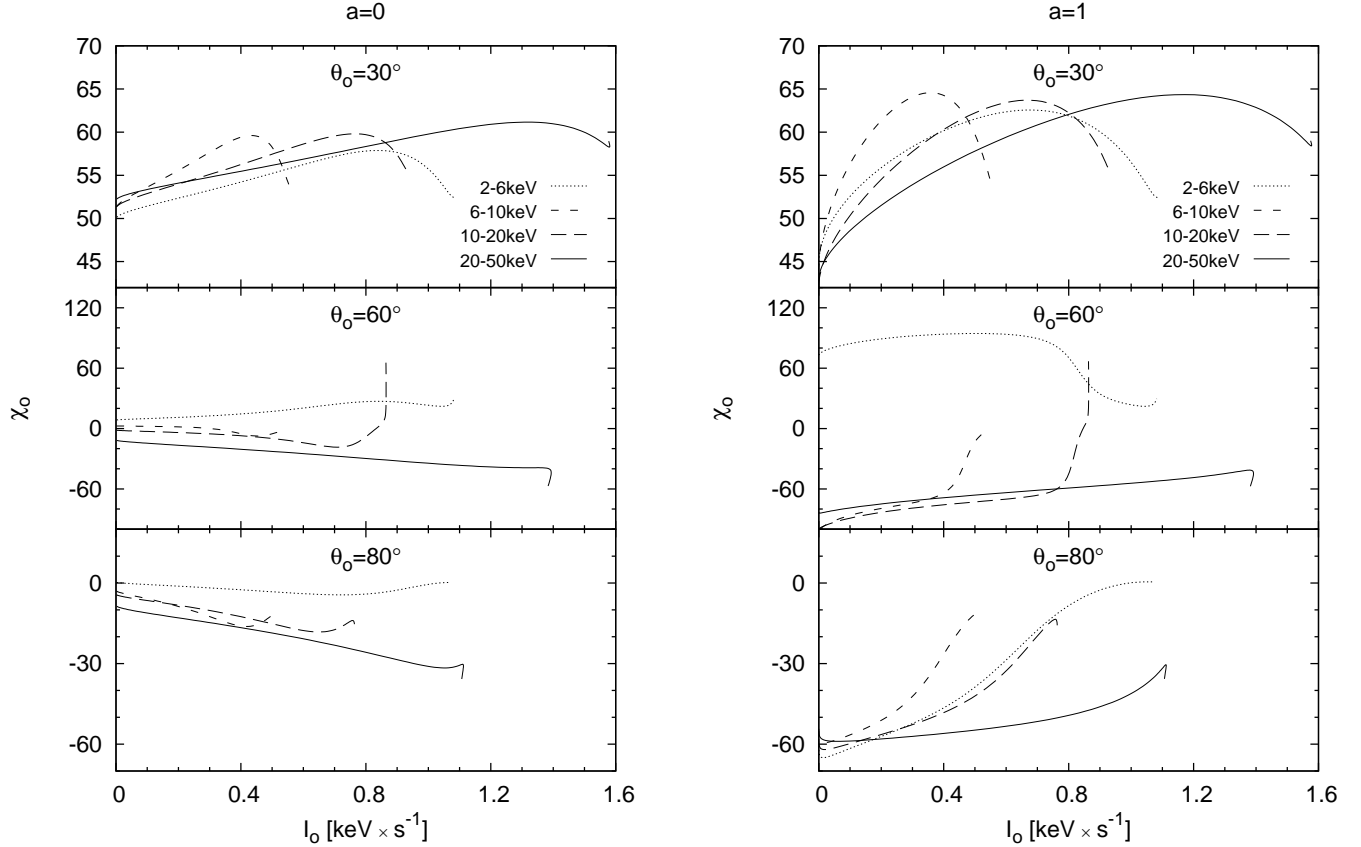


**Figure 12.** Dependence of the polarization angle at infinity on the total observed intensity. A polarization angle of  $0^\circ$  represents the direction perpendicular to the disk. The values for the energy ranges 2–6, 6–10, 10–20, and 20–50 keV for three different observer inclinations,  $\theta_o = 30^\circ$ ,  $60^\circ$ , and  $80^\circ$  (top to bottom panels) are shown. The height of the primary source increases with the total intensity from 0 to  $100 \text{ GM}/c^2$ . *Left:* The non-rotating Schwarzschild black hole case ( $a=0$ ). *Right:* The maximally rotating Kerr black hole case ( $a=1$ ).

dle and bottom panels in the same figure). The change in behavior is very well visible by rapid change of polarization angle with inclination in Figure 11. The transition happens at the inclination when the polarization above critical radius starts to dominate for higher inclinations. The transition depends on the lamp-post height and energy band and it can be either gradual or quite abrupt. Notice that there is no transition (or a very mild one) in the bottom panel in Figure 11 for the extreme Kerr black hole and for a very low height of the primary source. This is due to the fact that the inner region below the critical point still has large impact on the polarization at infinity even for very high inclinations. In this case also the dip in the dependence of the polarization degree on inclination is not so deep, see the dotted graphs of bottom middle panel in Figure 9.

For very high inclinations the polarization angle at infinity is determined by outer regions of the disk. Here relativistic effects are small enough so that the polarization at infinity is given by the local values in the disk. Because the incident and emission angles are very large in this area and for this inclination, the polarization angle will be  $0^\circ$  (or  $180^\circ$ ). The values in Figure 11 are smaller, mainly for high heights because the disk in our computations does not extend to infinity but up to  $1000 \text{ GM}/c^2$  and therefore the incident angle is smaller than  $90^\circ$  and

the local polarization angle decreases.

It is good to understand the behavior of the polarization for different lamp-post heights and observer inclinations, however, the height cannot be directly measured and to test the dependence on inclination we would need polarimetric observations of many AGNs. Therefore in the next sections we will use the dependence of the polarization on the directly measurable total intensity that can be observed at infinity. To this purpose we show the theoretical curves for different energy bands for the polarization degree in the right panel in Figure 9 and for the polarization angle in Figure 12. In these figures the height of the primary source increases with the total intensity.

## 7. OBSERVATIONAL PERSPECTIVES

### 7.1. Monte Carlo simulations of the detector response

The complex dependence of the polarization on the geometry of the system gives important insight in the emission process at work in accreting black holes. Many missions with the capability of measuring polarization are expected or are discussed for launch in the next few years and therefore it is important to investigate if the sensitivity is sufficient to perform polarimetry also of relatively faint sources like AGN. For this purpose, we developed a dedicated Monte Carlo software which is de-

scribed below.

Instruments able to measure polarization exploit the modulation which appears in the case of polarized radiation in the azimuthal response. Experimentally, this response, or modulation curve, is the histogram of the initial direction of photoelectron for photoelectric polarimeters (Bellazzini & Spandre, 2010) or that of the scattering direction for Compton devices (McConnell, 2010). If the impinging photons are polarized, the photoelectrons (or the scattered photons in the case of Compton instruments) are not isotropically distributed, but their azimuthal distribution on the plane orthogonal to the direction of incidence shows a cosine square modulation. The peak (or the minimum) corresponds to the direction of polarization, while the amplitude of the modulation is linearly proportional to the degree of polarization. The maximum modulation achieved for 100% polarized radiation is called modulation factor of the instrument  $\mu$  and it is in general a function of the energy.

In the following we will assume instruments based on a photoelectric polarimeter, the Gas Pixel Detector (GPD; Bellazzini & Muleri 2010). The systematic effects of GPD have been reported to be below 0.3% (Bellazzini & Spandre 2010), and therefore they can be neglected if the polarization degree is above  $\sim 1\%$ . In this hypothesis, the sensitivity of a polarimeter is only a matter of how many photons are collected. The number of photoelectrons emitted in each azimuthal angular bin is Poisson distributed and its fluctuations ultimately limit the capability to measure the amplitude of the modulation curve and, consequently, the polarization (Weisskopf et al. 2010).

The basic idea behind our Monte Carlo software is to derive the degree and the angle of polarization by generating test modulation curves, that is trial histograms representing the azimuthal distribution of photoelectrons. The entries in each histogram, one for each spectral interval of interest, is the number of collected photons in that energy band. The number of counts  $N_i$  in each angular bin  $i$  is distributed as a cosine square function, whose phase and amplitude are the angle of polarization and the product of the modulation factor and the degree of polarization averaged in the energy band, respectively. A Poisson noise  $\sqrt{N_i}$  is added in each angular bin. The modulation curve is fitted with a function  $\mathcal{M}(\phi) = A + B \cos(\phi - \phi_0)$ , where  $A$  and  $B$  are constants. The fit returns the “measured” angle of polarization  $\Phi_j = \phi_0$  and its error  $\sigma_{\Phi_j}$ , while the polarization degree  $\mathcal{P}_j$  (alongside with its error) is derived from the usual formula

$$\mathcal{P}_j = \frac{1}{\mu} \frac{\mathcal{M}_{max} - \mathcal{M}_{min}}{\mathcal{M}_{max} + \mathcal{M}_{min}} = \frac{1}{\mu} \frac{B}{B + 2A}. \quad (7)$$

The fit is repeated  $J$  times, e.g. 1000, adding a different Poisson noise contribution to the histogram for each trial. Eventually the expected (“measured”) degree and angle of polarization (and their errors) are derived by averaging the values obtained by the  $j$ -th trial,

$$\mathcal{P} = \overline{\mathcal{P}} \equiv \frac{1}{J} \sum_j \mathcal{P}_j, \quad \sigma_{\mathcal{P}} = \overline{\sigma_{\mathcal{P}}}, \quad \Phi = \overline{\Phi_j}, \quad \sigma_{\Phi} = \overline{\sigma_{\Phi_j}}. \quad (8)$$

This method was used by Dovčiak et al. (2008) to derive the sensitivity of next X-ray polarimetry missions

to the rotation of the plane of polarization in the emission from accreting Galactic black holes. In that case polarization was to be measured in quite narrow energy bands, about 1 keV, and therefore it was possible to define the average quantities required to generate the test modulation curves, e.g. the modulation factor, the angle and the degree of polarization. Instead here we need to study the sensitivity on a wider energy interval and therefore we present a different approach, initially proposed by Costa (private communication), which has also the advantage of taking into account the finite energy resolution of the instrument.

The simulation starts from the knowledge of the modulation factor, the spectrum of the source, the expected degree and the expected angle of polarization. They are calculated in  $K$  narrow spectral bins, typically 0.1 keV which is well below the energy resolution of the Gas Pixel Detector (about 1 keV at 6 keV). The values of the modulation factor, of the spectrum, of the degree and of the angle of polarization in the  $k$ -th spectral bin  $E_k$  will be named  $\mu_k$ ,  $F_k$ ,  $P_k$ ,  $\varphi_k$ , respectively. For each  $k$ -th bin in energy, we build a histogram with a cosine square modulation proportional to  $P_k \mu_k$  and a phase  $\varphi_k$ . The histograms have  $I$  angular bins between 0 and  $2\pi$ , e.g. 72 bins corresponding to intervals of 5 degrees, and the total number of elements is proportional to  $F_k$ . The value of the  $k$ -th element in the  $i$ -th angular bin  $H_{ki}$  is basically the fraction of the flux in the spectral bin  $E_k$  which causes a photoelectron to be reconstructed in the  $i$ -th angular direction (neglecting statistical fluctuations). So far this is not very different from the approach formerly presented, with the only difference that we define histograms in very narrow energy bands.

The finite spectral resolution of the instrument makes the measurement of the energy of the photon to be smeared around an average value. This causes a photon at energy  $E$  to be reconstructed as a photon at different energy  $\hat{E}$ , and the difference between  $E$  and  $\hat{E}$  depends on the energy resolution. The uncertainty on the energy measurement needs to be convolved with the response of the instrument, in particular with the dependence of the modulation factor on energy. As a matter of fact, completely polarized photons at energy  $E$  cause a modulation of amplitude  $\mu(E)$  which can be quite different from  $\mu(\hat{E})$ . To model properly the amplitude of the modulation, one should take into account that the instrument responds to polarization differently with the energy and that the energy is measured with a finite resolution. In our Monte Carlo simulations we include this degeneracy. We assume, and this is appropriate in most cases, that the effect of the finite energy resolution is limited to smear the energy of the event and that it does not act on the direction of emission of the photoelectron, namely on the polarization. Therefore we apply the blurring due to the finite spectral resolution to the spectra resolved in angular bins. Practically, this is done by taking the  $K$  values  $H_{k\bar{i}}$  for any angular bin  $i = \bar{i}$  and for  $k \in [0, K-1]$ , where we recall that  $k$  is the index running over the spectral bins. These  $I$  spectra are introduced in XSPEC as additional models and the response matrix of the instrument is used to apply a Gaussian smearing to them with the XSPEC tool `fakeit`. The results are *I pha* files which contain the number of counts  $N_{ki}$  col-

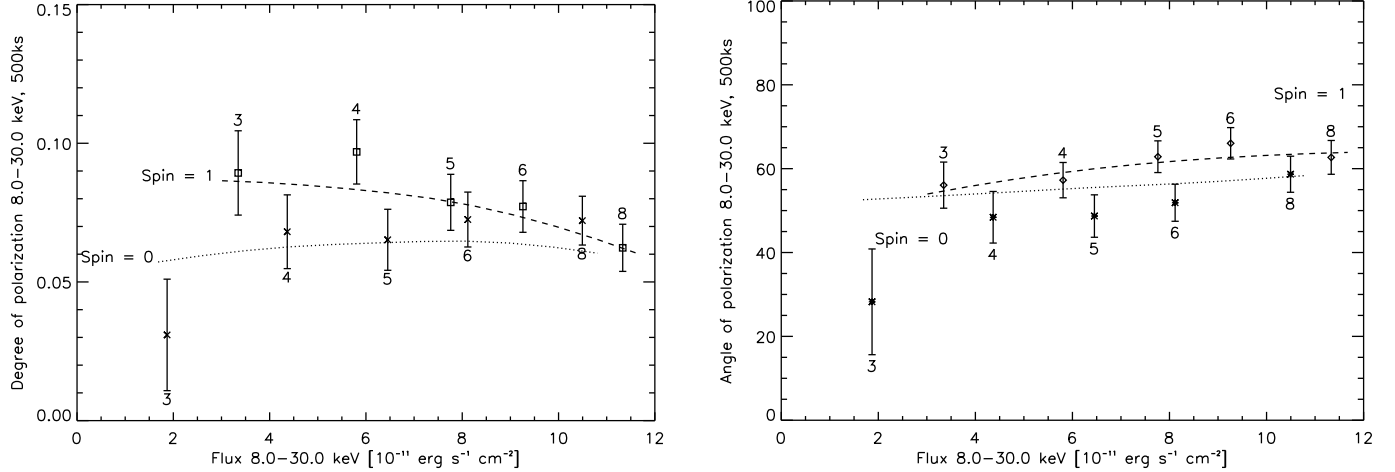


**Figure 13.** Correlation of the degree (left) and of the angle of polarization (right) with the flux for MCG-6-30-15. Each point corresponds to a different height of the source, specified within the figure (in units of  $GM/c^2$ ). It is assumed that each state of the source is observed for 500 ks with the Medium Energy Polarimeter on-board NHXM in the 8–30 keV energy interval. The dashed and the dotted lines are the expected dependency for spin 1 and spin 0, respectively.

lected in the angular bin  $i$  for each spectral bin  $E_k$  in the detector energy space.

The arrays  $N_{k'i}$  for any fixed value of  $k'$  and any value of  $i$  represent a sort of modulation curves defined in very narrow energy bands  $E_{k'}$  of 0.1 keV that we name “pseudo modulation curve” (because the Poisson noise has not been included yet). Any practical measurement will be performed in much larger energy intervals, of the order of a few keV. Therefore we build the pseudo modulation curves in any energy band of interest  $\Delta E_l$  by summing those histograms  $N_{ki}$  which are referred to spectral bins  $E_k$  contained in the interval  $\Delta E_l$ . This results in  $L$  pseudo modulation curves, as many as the number of intervals, which we name  $M_l$ , where we drop the subscript  $i$  (we implicitly assume the angular dependence being indicated by  $i$ ). The values of  $M_l$  take into account the effect of the finite energy resolution on the amplitude of the modulation and that the degree and the angle of polarization can change with energy, that is these quantities are assumed constant only on small intervals of 0.1 keV.

After that the pseudo modulation curves are generated, the Monte Carlo scheme proceeds as discussed above. In each  $\Delta E_l$  energy band, the software produces  $J$  trial modulation curves, which are calculated from the same pseudo modulation curves  $M_l$  but adding for each trial a different Poisson noise. Each trial modulation curve is fitted with the function  $\mathcal{M}(\phi) = A + B \cos(\phi - \phi_0)$ , and eventually the “measured” degree and angle of polarization are derived by averaging the values obtained by each trial; see equation (8). The value of the modulation factor used in each energy band to derive the polarization degree from the amplitude of the modulation (see equation 7) is obtained by weighting the dependency of  $\mu$  with energy on the spectrum of the source.

## 7.2. Results

The Monte Carlo scheme was used to investigate if polarimeters on-board next missions could detect distinctive signatures of the lamp-post model. A key characteristic of such a model is that the height of the illuminating source must change to explain the temporal variation of the source. This results also in a change of the observed

flux and polarization, as reported in right panel in Figure 9 and 12. Therefore our primary objective is to discuss if next missions will be able to find an evidence of the positive correlation between the degree of polarization and the flux.

### 7.2.1. Predictions for AGN case: MCG-6-30-15

First we model the case of Seyfert 1 galaxy MCG-6-30-15. From the simulations presented above we know how the flux and the polarization correlate, but we still need to associate the primary source height to a total flux measured in a certain state. Since we can not derive this normalization from the available information, we assume that the lowest flux state measured by Lee et al. (2000) corresponds to  $h = 3 GM/c^2$ . This choice, though arbitrary, is supported by conclusions of other authors, who suggest that the illuminating source is quite close to the central black hole. We assume that the observation inclination is  $30^\circ$  and that the black hole in MCG-6-30-15 is maximally rotating.

An interesting result expected on the basis of the lamp-post model is that the polarization usually increases with energy (see Figure 8). Therefore in the following we will take as an example the New Hard X-ray Mission (NHXM hereafter), which is dedicated to perform imaging, spectroscopy, and polarimetry in a wide energy interval extending from soft to hard X-rays (Tagliaferri et al., 2010a). NHXM will allow for polarimetry above 10 keV where the reflected radiation start to dominate the emission. In the focus of one of the four multilayer telescopes there will be alternatively placed two photoelectric polarimeters based on the Gas Pixel Detector, which are sensitive in the intervals 2–10 and 6–35 keV, and possibly a third Compton polarimeter which would extend the response up to 80 keV (Soffitta et al. 2010). Here we focus on the Medium Energy Polarimeter (MEP), the polarimeter that will be sensitive between 6 and 35 keV.

We show the correlations of the degree and of the angle of polarization with the flux in Figure 13. Both the flux and the polarization are integrated in the energy range 8–30 keV to avoid the iron line which is expected to be unpolarized. Each point represents an observation of 500 ks

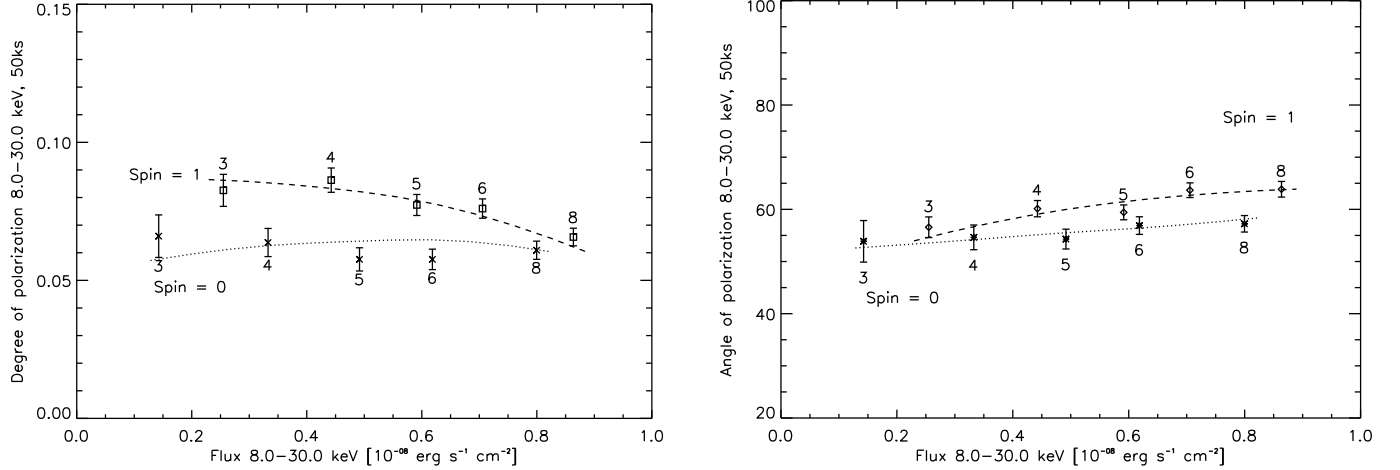


**Figure 14.** The same as Figure 13 but for the Galactic black hole system XTE J1650-500. It is assumed that each state of the source is observed for 50 ks with the MEP on-board NHXM in the 8–30 keV energy interval.

and corresponds to a different state of the source, that is a different height as indicated in the figure. Although the angle of polarization is almost constant with the flux, a certain evolution of the degree of polarization should be detectable. Moreover, we report for comparison the evolution of the polarization expected in the case of a Schwarzschild black hole to show that such evolution is somehow dependent on the spin of the central black hole.

#### 7.2.2. Predictions for Galactic black hole systems: XTE J1650-500

Features which can be regarded as due to reflection, such as relativistic iron lines, are observed in a number of Galactic black hole systems; see Miller (2007) for a review. There have been attempts to apply the light bending scenario also to these sources in analogy with the AGN case and therefore we discuss also the possibility to observe the correlation between the polarization and the flux in the case of Galactic objects.

We take as an example the transient black hole system XTE J1650-500 and associate the maximum flux measured by Rossi et al. (2005) to the a source height  $h = 8 GM/c^2$ , changing the source height between this value and  $h = 3 GM/c^2$ . We assume that the source spin is 1 and the observer inclination is  $30^\circ$ . We suppose to observe each state of XTE J1650-500 for 50 ks with the MEP on-board NHXM. The result is reported in Figure 14. In this case a significant detection could be reached with quite short observations.

## 8. DISCUSSION AND CONCLUSIONS

In this paper we have discussed the observational properties of the intensity of the emerging primary radiation component, the radiation component incident on the accretion disk, and the reflected radiation in the lamp-post geometry (the light bending model). We have extended our previous work on the subject and showed new results for polarization computations, including the unpolarized iron line complex in 2–10 keV energy range and the Compton hump at higher energy band (above 15 keV). We used our theoretical computations to model possible future observations by next-generation X-ray satellite missions equipped with an X-ray polarimeter on board.

For low inclinations we find that the polarization of the reflected radiation is diminished in the broad iron line energy region. For high inclinations, however, the situation is more complicated due to the shift of the iron edge; this effect enhances the observed polarization and it may balance the expected decrease. In principle the effect of lower polarization of the relativistic broad line region could be used to discriminate between the relativistically broadened iron line and the partial covering scenario, which are both proposed to explain the excess of flux in the spectra of black-hole accretion disks between 2–10 keV (see e.g. Miller et al. 2009). Note, however, that we did not try to estimate the behavior of the polarization in the partial covering scenario in this paper.

The polarization degree in a lamp-post geometry is higher at the highest studied energy band, 20–50 keV. This is a natural result coming from the fact that the primary source has a power-law spectrum with a negative index. Thus the best results for polarimetry of reflection spectra should be achieved in the Compton hump energy region. We also get higher polarization degree for large values of spin of the black hole, small height of the primary source, and low inclination of the observer.

As an example of the polarimetric sensitivity of next missions, we could assume the performance of the Gravity and Extreme Magnetism SMEX (GEMS; Jahoda, 2010; Black et al., 2010), which will be launched by 2014. However, the energy range of the polarimeters on-board GEMS will be limited between 2 and 10 keV, with the peak of the sensitivity being around 3–4 keV. Thus it will observe photons in a region where the iron (unpolarized) fluorescent line is prominent and the direct radiation from the corona largely dominates the reflected component. The reflected radiation is the only one polarized in our model. Consequently the expected degree of polarization is quite low, between 1 and 2% depending on the height of the illuminating source. Thus the signal could be more easily affected by even a small amount of polarization of some other origin, e.g. by Comptonized thermal emission in case of X-ray Black hole binaries (Dovčiak et al., 2008; Li et al., 2009; Schnittman & Krolik, 2009). Therefore we preferred to simulate observations of the polarization in higher energy

band.

In our model there were several assumptions and approximations that could affect the resulting polarization. First of all the primary radiation was unpolarized. It is clear that the effect this will have on our results will be most prominent in low energy bands, for higher lamp-post heights, low inclinations or small black-hole spins where primary emission is dominant (see Figure 7). Thus the polarization at low energies could be enhanced but determined by the primary source while the polarization at higher energies could be reduced.

In our computations we used the single scattering approximation for local polarization properties. The accuracy of this approximation depends on the energy. One can have an idea of the effect confronting Figure 1 (lower panel) and Figure 3 in Matt (1993). It follows from these figures that for energy below 10 keV results should not change much, while they could be different by about 25% in the 10 – 30 keV and by almost 40% in the 30 – 50 keV energy range.

We assumed a smooth equatorial disk. In case of a “rough” disk, with random ripples of the length much smaller than the length at which relativistic effects change considerably, the local polarization properties should be averaged over incident and emission angles. Because we average over these values anyway when integrating over the disk but including the relativistic effects it is hard to predict in a unique way how this will change the overall polarization at infinity. In case the disk is smooth but not strictly equatorial (warped disk but still close to the equatorial plane), the local geometry of scattering in the disk will be changed and thus the polarization at infinity will be changed as well, both dependent on the geometry of warping. In case of largely warped disks or non-aligned disks we expect different results mainly because the disk would be more illuminated at places closer to and facing the primary source, and because of the different local geometry of scattering and different values of the relativistic effects.

Our work is complementary to Schnittman & Krolik (2010) who assume a different geometry and structure of the corona. A direct comparison of their paper with our results is not easy because of different approximations adopted in these two works and the notorious sensitivity of polarization to details of the model. Nevertheless, the general set-up is similar in both scenarios and the level of expected polarization is comparable.

The behavior of the polarization degree and polarization angle in the light bending model is quite complex. Because the result depends on the interplay of several parameters, the polarization properties may be degenerate with respect to different parameter values (e.g. for larger heights we cannot distinguish a difference between a rotating and a non-rotating black hole). Nevertheless, when combined with spectral and timing observations, polarimetry is yet another important channel that can help us to uncover the physical parameters of the black-hole accretion disk systems, such as the black hole spin, the system inclination, and the height of the illuminating source.

The authors would like to thank anonymous referee for her/his comments that have lead to substantial improvement of the manuscript. We thank E. Costa, P. Soffitta, R. Bellazzini, and A. Brez for making available the sensitivity model of the Gas Pixel Detector for NHXM mission, and S. Bianchi for useful discussions. MD and VK acknowledge the Czech Science Foundation (ref. 205/07/0052) and the ESA PECS project (ref. 98040). The Astronomical Institute has been supported by the project LC06014 of the Centre for Theoretical Astrophysics in the Czech Republic. GM and FM acknowledge financial support from Agenzia Spaziale Italiana (ASI I/088/06/0). MD and RG are grateful for the support by the European Researchers Exchange program organized by the AS CR and the French CNRS.

## REFERENCES

- Agol, E., & Krolik, J. H. 2000, *ApJ*, 528, 161  
 Bellazzini, R., & Muleri, F. 2010, *NIMPA*, 623, 2  
 Bellazzini, R., & Spandre, G. 2010, in *X-ray Polarimetry: A New Window in Astrophysics*, eds. R. Bellazzini et al. (Cambridge University Press: Cambridge), 19  
 Bellazzini, R. et al. 2006, in *Space Telescopes and Instrumentation II: Ultraviolet to Gamma Ray*, Proc. of SPIE Conference, eds. M. J. L. Turner et al., Vol. 6266, 62663Z  
 Black, J. K. et al. 2010, *Proc. of SPIE Conference*, eds. M. Arnaud et al., Vol. 7732, 77320X-1  
 Blandford, R. D., Netzer, H., Woltjer, L., Courvoisier, T. J.-L., & Mayor, M. 1990, *Active Galactic Nuclei*, Saas-Fee Advanced Course 20 (Springer: Berlin)  
 Chandrasekhar, S. 1960, *Radiative transfer* (Dover: New York)  
 Connors, P. A., & Stark, R. F. 1977, *Nature*, 269, 128  
 Connors, P. A., Stark, R. F., & Piran, T. 1980, *ApJ*, 235, 224  
 Dabrowski, Y., & Lasenby, A. N. 2001, *MNRAS*, 321, 605  
 Dovčiak, M. 2004, PhD Thesis (Charles University: Prague), arXiv:astro-ph/0411605  
 Dovčiak, M. 2010, in *X-ray Polarimetry: A New Window in Astrophysics*, eds. R. Bellazzini et al. (Cambridge University Press: Cambridge), 95  
 Dovčiak, M., Karas, V., Martocchia, A., Matt, G., & Yaqoob, T. 2004a, in *RAGtime 4/5: Workshops on Black Holes and Neutron Stars*, eds. S. Hledík & Z. Stuchlík (Silesian University: Opava), 33  
 Dovčiak, M., Karas, V. & Matt, G. 2004b, *MNRAS*, 355, 1005  
 Dovčiak, M., Muleri, F., Goosmann, R. W., Karas, V., & Matt, G. 2008, *MNRAS*, 391, 32  
 Dumont, A.-M., Abrassart, A., & Collin, S. 2000, *A&A*, 357, 823  
 Fabian, A. C. 2008, *AN*, 329, 155  
 Fabian, A. C., Iwasawa, K., Reynolds, C. S., & Young, A. J. 2000, *PASP*, 112, 1145  
 Fabian, A. C., Pounds, K. A., & Blandford, R. D. 2004, *Frontiers of X-ray Astronomy* (Cambridge University Press: Cambridge)  
 Frank, J., King, A., & Raine, D. J. 2002, *Accretion Power in Astrophysics* (Cambridge Univ. Press: Cambridge)  
 Henri, G., & Petrucci, P. O. 1997, *A&A*, 326, 87  
 Jahoda, K. 2010, *Proc. of SPIE Conference*, eds. M. Arnaud et al., Vol. 7732, 77320W  
 Karas, V. 2006, *AN*, 327, 961  
 Kato, S., Fukue, J., & Mineshige, S. 1998 *Black-hole Accretion Disks* (Kyoto University Press: Kyoto)  
 Krolik, J. H. 1999, *Active Galactic Nuclei: From the Central Black Hole to the Galactic Environment* (Princeton University Press: Princeton)  
 Laor, A., Netzer, H., & Piran, T. 1990, *MNRAS*, 242, 560  
 Lee, J. C. et al. 2000, *MNRAS*, 318, 857  
 Li, Li-Xin, Narayan, R., & McClintock, J. E. 2009, *ApJ*, 691, 847  
 Martocchia, A., Karas, V., & Matt, G. 2000, *MNRAS*, 312, 817  
 Martocchia, A., & Matt, G. 1996, *MNRAS*, 282, L53  
 Matt, G. 1993, *MNRAS*, 260, 663  
 Matt, G. 2006, *AN*, 327, 949  
 Matt, G., Perola, G. C. & Piro, L. 1991, *A&A*, 247, 25

## ACKNOWLEDGMENTS



- McConnell, M. L. 2010, in *X-ray Polarimetry: A New Window in Astrophysics*, eds. R. Bellazzini et al. (Cambridge University Press: Cambridge), 11
- Miller, J. M. 2007, *ARA&A*, 45, 441
- Miller, L., Turner, T. J., & Reeves, J. N. 2009, *MNRAS*, 399, L69
- Miniutti, G., & Fabian, A. C. 2004, *MNRAS*, 349, 1435
- Niedźwiecki, A., & Miyakawa, T. 2010, *A&A*, 509, A22
- Niedźwiecki, A., & Życki, P. T. 2008, *MNRAS*, 386, 759
- Petrucchi, P. O., & Henri, G. 1997, *A&A*, 326, 99
- Remillard, R. A., & McClintock, J. E. 2006, *ARA&A*, 44, 49
- Rossi, S., Homan, J., Miller, J. M., & Belloni, T. 2005, *MNRAS*, 360, 763
- Schnittman, J. D., & Krolik, J. H. 2009, *ApJ*, 701, 1175
- Schnittman, J. D., & Krolik, J. H. 2010, *ApJ*, 712, 908
- Soffitta, P. et al. 2010, in *Space Telescopes and Instrumentation 2010: Ultraviolet to Gamma Ray*, Proc. of SPIE Conference, eds. M. Arnaud et al., Vol. 7732, 77321A
- Swank, J., Kallman, T., Jahoda, K., Black, K., Deines-Jones, P., & Kaaret, P. 2010, in *X-ray Polarimetry: A New Window in Astrophysics*, eds. R. Bellazzini et al. (Cambridge University Press: Cambridge), 251
- Tagliaferri, G. et al. 2010a, in *The Extreme Sky: Sampling the Universe above 10 keV*, Proceedings of Science (arXiv:1004.2691)
- Tagliaferri, G. et al. 2010b, in Bulletin of the American Astronomical Society (HEAD meeting No. 11), 41, 741
- Weisskopf, M. C., Elsner, R. F., & O'Dell, S. L. 2010, in *Space Telescopes and Instrumentation 2010: Ultraviolet to Gamma Ray*, Proc. of SPIE Conference, eds. M. Arnaud et al., Vol. 7732, 77320E (arXiv:1006.3711)
- Życki, P. T., Ebisawa, K., Niedźwiecki, A., & Miyakawa, T. 2010, *PASJ*, 62, 5